Vibration-induced streaming flow near a sharp edge: Flow structure and instabilities in a large span of forcing amplitude

Geyu Zhong, Yingwen Liu, Xiaofeng Guo, Laurent Royon, Philippe Brunet

Vibration-induced streaming flow near a sharp edge: Flow structure and instabilities in a large span of forcing amplitude

Geyu Zhong [1,2] Yingwen Liu [1] Xiaofeng Guo [2,*] Laurent Royon [2,†] and Philippe Brunet [3,‡]

[1] *Key Laboratory of Thermo-Fluid Science and Engineering of MOE, School of Energy and Power Engineering, Xi'an Jiaotong University, Xi'an 710049, Shaanxi, China*

[2] *Université Paris Cité, LIED, UMR 8236, CNRS, F-75006 Paris, France*

[3] *Université Paris Cité, MSC, UMR 7057, CNRS, F-75006 Paris, France*

(Received 1 May 2022; accepted 24 January 2023; published 13 February 2023)

The steady streaming generated near solid walls by the periodic forcing of a viscous fluid is known to be strongly enhanced near sharp structures, owing to centrifugal effects that lead to the generation of an intense jet from the sharp tip. This flow has been shown to provide efficient active mixing in microchannels, due to strong transverse velocity. The forcing is often prescribed by acoustic transducers, but it can also be generated from low-frequency time-periodic flow ensured by mechanical vibrations. In this paper, we study the flow structure generated by low-frequency forcing (typically 10 Hz) around a sharp tip. Using direct numerical simulations, we extract both the time-periodic and steady responses within a large span of amplitude of vibrations. When the amplitude is smaller than the tip radius of curvature, we recover the flow structure observed at higher frequencies (>1 kHz) in previous studies, namely, an intense symmetric central jet and a quadratic dependence for the characteristic streaming velocity with the oscillating velocity $v_s \sim v_a^2$. At higher amplitudes, such a scaling no longer holds and the streaming flow pattern loses its left-right symmetry. We then analyze the mechanisms of the instability from the careful examination of the instationary flow fields, and we propose possible mechanisms for such a flow transition involving the coupling between the streaming jet and instationary vorticity.

DOI: 10.1103/PhysRevE.107.025102

I. INTRODUCTION

The phenomenon of *steady streaming* describes the time-averaged flow originating from the viscous dissipation of time-periodic flow oscillations, either in the bulk or near walls or boundaries. These vibrations can either be of mechanical or acoustical nature, and in the later case the steady flow is denoted as *acoustic streaming* (AS). When an acoustic wave propagates through a fluid medium, the acoustic streaming is generated along the direction of propagation [1], and this flow is denoted as *Eckart streaming* [2]. It has been related to the Reynolds stress [3] that is associated to the unsteady component of the flow. For low viscous liquids like water, and relatively low frequency (<1 MHz), viscous dissipation mainly occurs near walls and boundaries, where the no-slip boundary condition induces strong velocity gradients. This is generally denoted as *Rayleigh-Schlichting streaming* [4,5] and can take the form of a periodic array of vortices of typical size equal to a quarter of the acoustic wavelength [6]. When boundaries offer sharp structures, intense streaming flow is observed near the highly curved tips. The origin of this intense streaming has been attributed to that the oscillating velocity experiences a sharp change of direction in the tip vicinity [7].

In an applied viewpoint, low-frequency vibrations are ubiquitous in numerous applications ranging from common household devices, transportation vehicles, ocean devices, industry machines, to human motions. In addition to harvesting vibration energy by piezoelectric effects [8–10], it has also been exploited as a possible way to enhance mass [11,12] and heat [13] transfer via the streaming vortices generated by this periodic forcing. In this prospect, a significant advantage of low-frequency actuation is the simplicity of the required instrumentation, which is in line with the recent trends to develop low-cost millifluidic or microfluidics lab-on-a-chip systems for various applications [14].

Intense streaming jets produced by sharp structures (also denoted as sharp-edge acoustic streaming, SEAS) were first reported by Huang and coauthors [15–17]. Then, Ovchinnikov *et al.* provided the first theoretical study [7] with both analytical relationships and numerical results. The phenomenon was later investigated through various applied situations [18–20], and recently revisited in both experimental and theoretical aspects [11,21–23]. Compared to Rayleigh streaming in usual (micro)channels [1], SEAS allows for a broader choice of acoustical or mechanical vibration sources, including those of substantially lower frequency f and thus with acoustic wavelength λ much larger than the size of the fluid container.

So far, most previous investigations on SEAS were conducted at a forcing frequency within a range from a few kHz [11,15–17,21,22] to almost 1 MHz [23], hence, a typical thickness for the viscous boundary layer (VBL), $\delta = \sqrt{2\nu/\omega}$ ranging roughly from 1 to 50 μm for water, where ν and ω

*xiaofeng.guo@u-paris.fr
†laurent.royon@univ-paris-diderot.fr
‡philippe.brunet@univ-paris-diderot.fr

represent the kinematic viscosity and angular frequency of the oscillation, respectively. Since a necessary condition to generate SEAS is to design structures with local curvature radius r_c significantly smaller than δ, this phenomenon was so far restricted to photolithographic-made microchannels with clean-room requirements. In this sense, the opportunity to exploit low-frequency vibrations would broaden the tip sharpness condition, and hence would enable to design sharp-edged structures using inexpensive and more conventional ways [machining tools, laser cutting, three-dimensional (3D) printing ...]. Also, the possibility of using more resistant materials like metal should push a major step forward towards real-field applications.

From a quantitative viewpoint, previous investigations showed that the magnitude of the streaming flow, often quantified by the maximal streaming velocity in the direction perpendicular to the channel walls, was proportional to the square of the vibration velocity v_a: $v_{sy,\max} \sim v_a^2$. Prior to quantitative checking within a large span of liquid and geometrical parameters [22], an analytical study showed that the magnitude of the streaming flow scaled as $v_s \sim \frac{v_a^2 h}{\nu}$ for infinitely sharp structures [7], where h is a typical height of the structure. Considering instead the wave amplitude $A = \frac{v_a}{2\pi f}$, this yields $v_s \sim \frac{A^2 f^2 h}{\nu}$. Hence, in order to keep strong enough streaming flow when operating at frequencies as low as 10 Hz, like those prevailing in our study, the amplitude A should then be taken within a range of values considerably higher than those for acoustic forcing with f within the kHz range or higher.

Consequently, contrary to previous studies on SEAS, the amplitude of the low-frequency vibrations A could be significantly larger than both r_c and δ. When operating within this unusual parameter range, the nonstationary (time-periodic) flow field is susceptible to show a different spatial pattern from that observed at relatively low forcing ($A < r_c, A < \delta$). Let us mention that experimentally, such vibrations can be conveniently generated by usual shakers or loudspeakers [24]. The response of such large amplitude forcing can induce instationary flows with separation or complex shedding modes, especially in the vicinity of sharp structures [25,26]. These instationary flows of scale larger than the typical VBL thickness are susceptible to interact with and to modify the symmetric y-oriented streaming jet. Therefore, several fundamental questions are to be answered:

(i) Can the microfluidics setup utilized in previously reported SEAS be widened to millimeter-wide channels where the fluid would be efficiently actuated by lower-frequency vibrations (typically around 10 Hz)?

(ii) If yes, what are the conditions to generate strong enough streaming? How does the flow then behave?

(iii) To which extent the streaming flow would keep the symmetrical shape found at relatively low amplitude, and would the relationship $v_{sy,\max} \sim v_a^2$ hold if A is no longer smaller than r_c or δ ?

This paper aims to address the above questions with numerical simulations of the Navier-Stokes (NS) equations. To better comprehend SEAS at such low frequency, a numerical scheme is established for a sharp-edged channel with typical width ranging from a few mm to several cm, with the resolution of the full NS equations within the whole domain.

Different vibration velocities v_a (or amplitude $A = \frac{v_a}{2\pi f}$) at a frequency $f = 10$ Hz are prescribed. Time-averaged velocity fields, maximum streaming velocity ($v_{s,\max}$), along with different streaming vortices patterns are extracted to characterize and quantify SEAS. Different flow regimes are identified and discussed, via analyses of streaming velocity fields and vorticity maps, also via the extraction of the instationary flow field and of the time evolution of flow kinetic energy. Following the presentation of our results, we discuss plausible mechanisms for the observed flow pattern and associated quantitative trends.

II. THEORETICAL BACKGROUND AND NUMERICAL MODEL

A. Equations and theory

The fundamental equations governing acoustic or vibration-induced streaming are well documented [3,27–32]. We summarize them thereafter. Our study addresses situations where the wavelength is large compared to the typical dimensions of the channel (length L or width H), so that $\lambda \gg (L, H)$, and at small enough vibration velocity with Mach number $\mathrm{Ma} = v_a/c \ll 1$, so that the fluid can be treated as being incompressible.

With the above assumptions and without external body forces nor heat sources, and for an isotropic homogeneous fluid, the mass and momentum conservation equations governing the flow are

$$\nabla \cdot \mathbf{v} = 0, \tag{1}$$

$$\rho \frac{\partial \mathbf{v}}{\partial t} + \rho(\mathbf{v} \cdot \nabla)\mathbf{v} + \frac{1}{\rho}\nabla p = \mu \nabla^2 \mathbf{v}, \tag{2}$$

where ρ is the liquid density, p the pressure field, and $\mathbf{v}$ the velocity field. Bold and normal font styles, respectively, represent vectorial and scalar quantities.

To investigate on steady streaming flows generated by periodic forcing (acoustic or mechanical), the velocity and pressure fields are generally decomposed as

$$\mathbf{v} = \mathbf{v}_0 + \mathbf{v}_\omega + \mathbf{v}_s, \quad \text{with } \mathbf{v}_\omega = \mathrm{Re}(\mathbf{v}_a e^{i\omega t}), \tag{3}$$

$$p = p_0 + p_\omega + p_s, \quad \text{with } p_\omega = \mathrm{Re}(p_a e^{i\omega t}), \tag{4}$$

where $\mathbf{v}_0$, $\mathbf{v}_\omega$, and $\mathbf{v_s}$ are, respectively, the unperturbed, the oscillating, and the time-averaged streaming component of the velocity. $\mathbf{v_a}$ is the amplitude of vibration velocity. Since the unperturbed flow is taken static (no mean directional flow), $\mathbf{v}_0 = \mathbf{0}$. Similarly, p_0, p_ω, and p_s are, respectively, the reference, the oscillating, and steady pressure associated to streaming flow, and p_a is the amplitude of the oscillating pressure field. The reference pressure is taken equal to the atmospheric one: $p_0 = p_{\mathrm{atm}}$.

Following the above decomposition, the governing momentum equation can be transformed into Eqs. (5) and (6) [21] by gathering time-periodic and steady terms into two distinct equations:

$$i\omega \mathbf{v}_a + (\mathbf{v}_s \cdot \nabla)\mathbf{v}_a + (\mathbf{v}_a \cdot \nabla)\mathbf{v}_s = -\frac{1}{\rho}\nabla p_a + \nu \nabla^2 \mathbf{v}_a, \tag{5}$$

$$(\mathbf{v}_s \cdot \nabla)\mathbf{v}_s + \frac{1}{2}\mathrm{Re}[(\mathbf{v}_a \cdot \nabla)\mathbf{v}_a^*] = -\frac{1}{\rho}\nabla p_s + \nu \nabla^2 \mathbf{v}_s. \tag{6}$$

One can notice the nonlinear terms of velocity contained in these two equations. After time averaging Eq. (6), a body force $\mathbf{F}_s$ is introduced to account for the nonlinear effects of vibrations, as shown in Eq. (7). As the driving force generating steady-state streaming, the force term can be expressed as Eq. (8):

$$(\mathbf{v}_s \cdot \nabla)\mathbf{v}_s = \frac{1}{\rho}(\mathbf{F}_s - \nabla p_s) + \nu\nabla^2\mathbf{v}_s, \tag{7}$$

$$\mathbf{F}_s = -\frac{\rho}{2}\langle \mathrm{Re}[(\mathbf{v}_a \cdot \nabla)\mathbf{v}_a{}^*]\rangle, \tag{8}$$

where the operator $\langle \dots \rangle$ stands for a time averaging over one period of oscillation $1/f$. One can deduce the force is high around sharp edges where v_a shows strong variations both in its amplitude, due to the no-slip condition at the wall, and in its direction due to a centrifugal effect, already mentioned in previous studies [7,21]. Therefore, similarly to studies at higher frequencies, the bending of the vibrating flow trajectories near the sharp edge is also the origin of the strong streaming at Hz-level frequencies.

To analyze the flow, the perturbation theory (PT) constitutes a common framework [3,27–32], under the assumption that $\|\mathbf{v}_s\| \ll \|\mathbf{v}_a\|$ and $p_s \ll p_a$, i.e., that the streaming velocity is of considerably lower magnitude than the forcing velocity [6,7,16,19,30–34]. By comparing with calculations achieved in the PT framework [7], nonlinear terms taking into account the coupling between $\mathbf{v}_a$ and $\mathbf{v}_s$ in Eq. (5) cannot be ignored in this study, which is also the case for the streaming advective term $(\mathbf{v}_s \cdot \nabla)\mathbf{v}_s$ in Eqs. (6) and (7). Given the strong streaming which can be generated near sharp edges [7,21], we have to dismiss these simplifying assumptions. Instead, we opt for a numerical scheme in which the NS equations are fully solved.

Furthermore, although including more terms than the PT, the decomposition proposed in Eqs. (5) and (6) is only valid for a reduced range of amplitude. Actually, like in most frameworks of acoustic or vibration streaming, the term $(v_\omega \cdot \nabla)v_\omega$ has been neglected in Eq. (5). Since the sharp edge adds a transverse component to (v_ω) and makes the flow being nonparallel, this assumption remains valid if $|(v_\omega \cdot \nabla)v_\omega)| \ll |\partial_t v_\omega|$. This condition defines a dimensionless number R_ω that compares the relative importance of convection and instationarity related to the oscillating flow:

$$R_\omega = \frac{|v_\omega|}{2r_c\omega} \tag{9}$$

obtained by taking $2r_c$ as the typical length scale over which the oscillating field evolves. The condition to neglect $(v_\omega \cdot \nabla)v_\omega$ then reads as $R_\omega = \frac{A}{2r_c} \ll 1$. In the following, we shall see that this condition is not fulfilled within a consequent range of amplitude. In particular, this leads to nonpurely harmonic oscillating flow since the term $(v_\omega \cdot \nabla)v_\omega$ induces higher-order components. This is one of the original aspects of our study, and the reason why we opted for simulations where the full Navier-Stokes equation is considered.

Let us mention recent studies allowing to address streaming and coupled effects under relatively large amplitude vibrations, by decomposing the velocity, density, and pressure fields into fast (vibrational) and slow (hydrodynamics and thermal) dynamics (see, e.g., Michel and Chini [35], Das *et al.* [36], and Bruus *et al.* [37]).

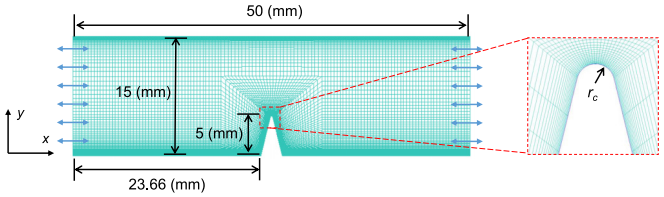

FIG. 1. Geometry of the computational domain, sketched in the left inset, together with a magnified view around the sharp-edge tip on the right inset. The angle of the tip is $\alpha = 30^\circ$ with its curvature diameter $2r_c$ ranging between 0.01 and 0.6 mm (here shown for 0.3 mm).

B. Numerical model and parameters

To compute the streaming flow, mass conservation and Navier-Stokes equations are solved directly with finite-volume method using the software ANSYS™ FLUENT. The geometrical parameters of the computational domain, representing the channel with a symmetrical triangular wedge with sharp tip, are detailed in Fig. 1. The computational model is established as being two dimensional, while the length (L) and the width (H) of the channel domain are 50 and 15 mm, respectively. These dimensions are shown to be large enough to avoid wall and edge effects since the streaming flow field is restricted to a much smaller area. The sharp edge is located at the middle of the channel length. Its tip angle is set to $\alpha = 30^\circ$, which represents a value generating relatively strong streaming [21] and its curvature diameter is taken equal to four different values $2r_c = 0.03$, 0.1, 0.3, and 0.6 mm. Water is chosen as the working fluid with constant density and kinematic viscosity ($\rho = 1000$ kg/m^3 and $\nu = 10^{-6}$ m^2/s) under standard operating conditions (20 °C). The frequency of oscillation is set to $f = 10$ Hz (with corresponding period T), which yields $\delta = 0.178$ mm for water. Previous studies [21] investigated the influence of r_c, evidencing a stronger streaming velocity for smaller tip radius, with all other parameters being invariant. This influence was found to be especially pronounced in the range $r_c \simeq \delta$. Hence, our study encompasses different situations where r_c/δ takes a value much smaller than unity ($\simeq$0.0842), smaller than unity ($\simeq$0.28), almost equal to unity ($\simeq$0.824), and larger than unity ($\simeq$1.685). Strictly speaking, only the first three cases should really be considered as SEAS. The last case is for sake of comparison regarding streaming intensity and flow pattern around a nonsharp structure.

The boundary condition (BC) at the inlet (left end of the channel) imposes a time-periodic velocity with $v_x = v_a \sin(2\pi f t + \varphi_0)$ along the horizontal direction and $v_y = 0$ along the vertical one (the initial phase $\varphi_0 = 0$ in most simulations of this study). The right end (outlet) is assigned with a condition of pressure fixed at $p_0 = p_{\mathrm{atm}}$, similarly to our previous studies [12,21]. The referred time-periodic velocity profiles at boundaries can be considered as in-phase for two reasons: (i) the flow is incompressible and (ii) the acoustic wavelength λ is much larger than the channel size. Originally,

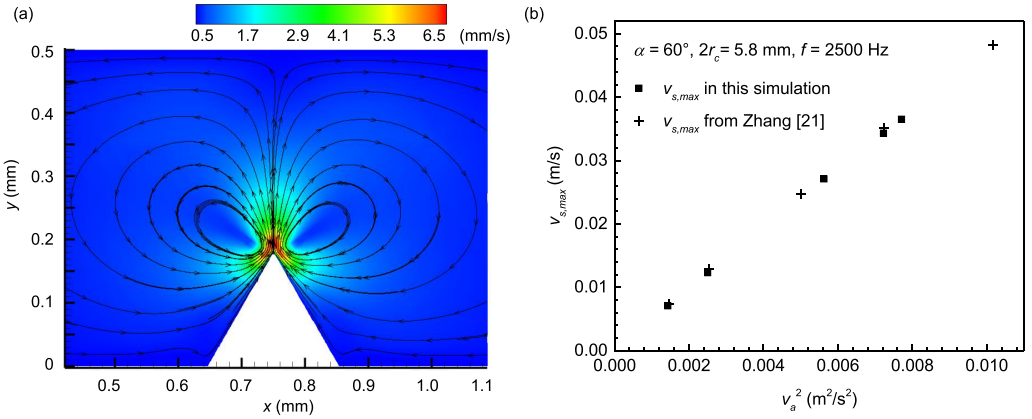

FIG. 2. Model validation. (a) Typical streamlines pattern and velocity field in SEAS, very similar to Fig. 3 in the study by Zhang *et al.* [21]. The parameters in this case are $\alpha = 60^\circ$, $2r_c = 5.8\,\mu$m, $f = 2500$ Hz, and $v_a = 37.8$ mm/s. (b) Comparison of numerical results between $v_{s,\max}$ and v_a^2 with published data (cross points) from Zhang *et al.* [21].

the choice of these BCs was motivated by allowing an additional constant flow rate in a easier way. For lateral walls of the computational domain as well as the sharp-edge boundaries, a condition of no slip ($\vec{v} = \vec{0}$) is prescribed. Let us note that we repeated some of our experiments with alternative BCs prescribing a time-periodic velocity with $v_x = v_a \sin(2\pi f t + \varphi_0)$ along the horizontal direction *both at the inlet and the outlet*, by constraining the left-right symmetry in the BCs. The purpose of these additional runs is to evidence that both BCs yield comparable results, both qualitatively and quantitatively, and to dismiss boundary conditions as a possible origin for asymmetric flow patterns. In the Supplemental Material [38], we show that results obtained with both BCs are qualitatively and quantitatively similar.

Furthermore, we validated and checked that our results are independent on the mesh refinement and time step, by comparing with simulations and experiments previously obtained in our group [21]. A structured mesh is employed with refined discretization in the vicinity of sharp edge and walls. Besides, each period is discretized into 100 time steps. After 150 periods, a steady streaming velocity field is found to be established, for all conditions investigated in this study. We thus consider the full establishment of a quasisteady SEAS after this reference time duration, though under some conditions a steady state is reached after a much shorter duration.

C. Model validation

With the assumptions of incompressibility and large acoustic wavelength, the momentum conservation equations presented above remain valid within a large range of frequency, typically from a few Hz (so that the VBL thickness δ is smaller than the channel width H) to several hundreds of kHz (so that $\lambda \gg H$ and L). Therefore, our numerical method is validated by checking its agreement with previous experimental results in a microchannel geometry by Zhang *et al.* [21], obtained at $f = 2500$ Hz, $\alpha = 60^\circ$, $2r_c = 5.8\,\mu$m, with water as the liquid and for various values for v_a. Figure 2 shows both a typical example of the streaming field, shown as velocity color maps and streamlines, obtained with the current numerical scheme [Fig. 2(a)], and the maximal value of the streaming flow $v_{sy,\max}$ along the y axis in both our current scheme and results obtained in Zhang *et al.* [21] for experiments and numerical simulations with finite-element software COMSOL in the same conditions. The very good agreement between the different series of data provides an indisputable validation of the numerical scheme used in this study.

We then use the same numerical scheme to quantitatively investigate the case of 10 Hz within a longer and wider channel. The main physical quantities related to geometrical, fluidic, and vibrational properties are listed in Table I.

III. RESULTS

A. Velocity and vorticity fields

We first describe the structure of the streaming flow at a semiquantitative level, by extracting the velocity and vorticity fields. For each value of curvature diameter $2r_c$ between 0.03 and 0.6 mm, the forcing velocity v_a is varied between 0.01 and 0.08 m/s. By opting for $f = 10$ Hz, it yields A values between 0.159 and 1.27 mm. Therefore, A can be comparable to or much larger than the two characteristic lengths r_c and $\delta = 0.178$ mm.

Figure 3 shows typical flow structures for various values of v_a (or A). Figure 3(a) corresponds to relatively low forcing amplitude, in the range $A \lesssim r_c$ and $A \lesssim \delta$, where the streaming flow remains symmetric. Figure 3(b) corresponds to a slightly larger amplitude ($A \gtrsim r_c$ and $A \gtrsim \delta$), and one can perceive the first signs of a left-right asymmetry (mainly visible in the outer streamlines), as well as two smaller vortices beside the sharp edge, in together with the two main large vortices. Figure 3(c) corresponds to a large amplitude ($A > r_c$ and $A > \delta$), and the streaming flow is strongly asymmetric. The transition is observed after a transient phase, described in more details later, during which the asymmetry progressively appears and amplifies in time. The transient roughly lasts a few seconds (or a few tens of periods), in effective computational time.

We first check if this symmetry breaking corresponds to an intrinsic hydrodynamic effect, rather than being caused

TABLE I. Main parameters used of the simulation.

Frequency f(Hz)	Forcing velocity v_a (m/s)	Curvature diameter $2r_c$ (mm)	Purpose
2500	0.0378	0.0058	Model validation
10	0.001–0.08	0.03–0.6	Parametric study

by numerical artifacts. Such an artifact could be due to that, while the forcing is supposedly homogeneous, the boundary conditions prescribed at the left and right ends of the channel are different. Therefore, we check if the side where the bigger vortex grows is always the same (hence due to a bias) or if it depends on the initial forcing conditions. Hence, we repeated the simulations under different initial phase shift φ_0. It turns out that the right or left side of the bigger vortex is strongly dependent on φ_0 (see Fig. 1 in the Supplemental Material [38]). The large vortex can also be observed on the left side if the initial phase shift $\varphi_0 = 3\pi/2$. Therefore, since the side where the flow grows stronger is highly influenced by initial conditions, it corresponds to an intrinsic effect and does not reflect any asymmetry of the system itself.

Also, to check that this instability is not induced by the finite width of the channel, we repeated the calculations for different geometries where the width was changed from 20 mm to 25, 40, and 60 mm. For the parameters investigated, no changes in the flow structure and magnitude of the symmetry breaking could be noticed (see Fig. 2 in the Supplemental Material [38]), evidencing the intrinsic character of the instability-induced asymmetry.

Finally, we check that the instability also appears for a different tip angle, which should emphasize the generic character of the instability. We repeat the simulations with $\alpha = 60^\circ$ and it turns out that the instability is also observed, although above a higher threshold in v_a. The different velocity maps are presented in the Supplemental Material [38] (Fig. 3).

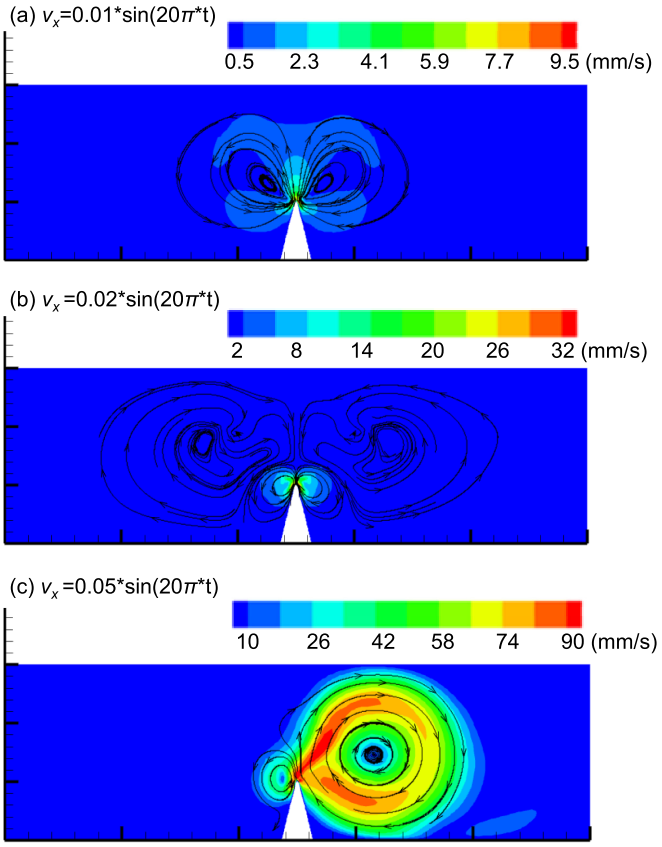

FIG. 3. Steady streaming flow field for various forcing velocities/amplitude at $f = 10$ Hz. (a) $v_a = 0.01$ m/s ($A \simeq 0.159$ mm), (b) $v_a = 0.02$ m/s ($A \simeq 0.318$ mm), and (c) $v_a = 0.05$ m/s ($A \simeq 0.796$ mm). A symmetric pair of vortices around the sharp edge is observed under weak forcing velocity v_a, while the flow field turns to be asymmetric at higher forcing velocities, when A is significantly larger than r_c (here = 0.15 mm) and δ (= 0.178 mm).

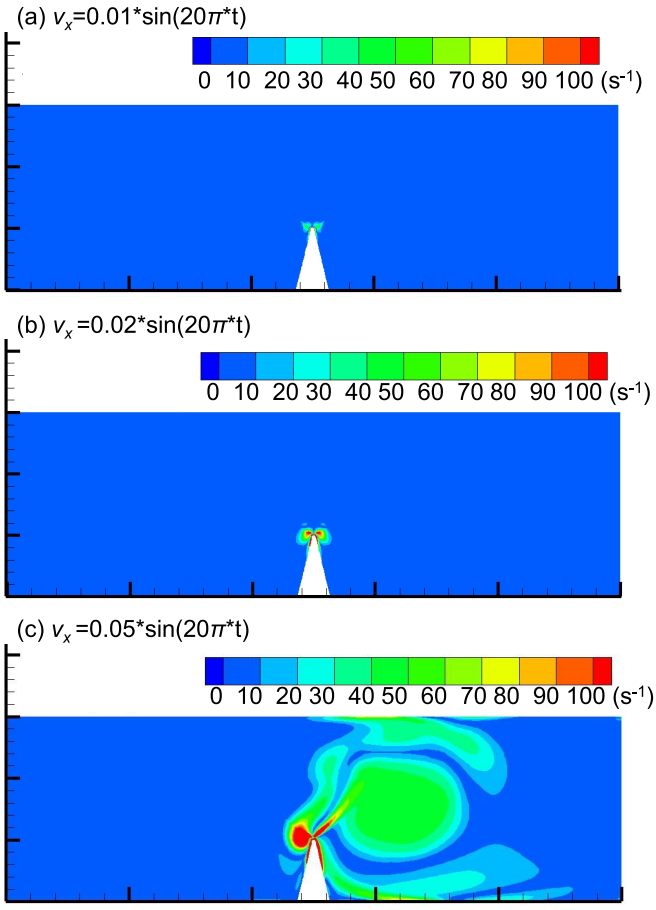

FIG. 4. Steady streaming vorticity field for different forcing velocities (same values as Fig. 3). (a) $v_a = 0.01$ m/s (maximum value = 203 s^{-1}), (b) $v_a = 0.02$ m/s (maximum vorticity = 755 s^{-1}), and (c) $v_a = 0.05$ m/s (maximum vorticity = 2506 s^{-1}), extracted from 15–15.1 s after the computational initial time, i.e., after 150 periods. For sake of comparison, the scales of the color maps are the same for the three situations, i.e., with maximum at 100 s^{-1} though the vorticity can locally take higher values.

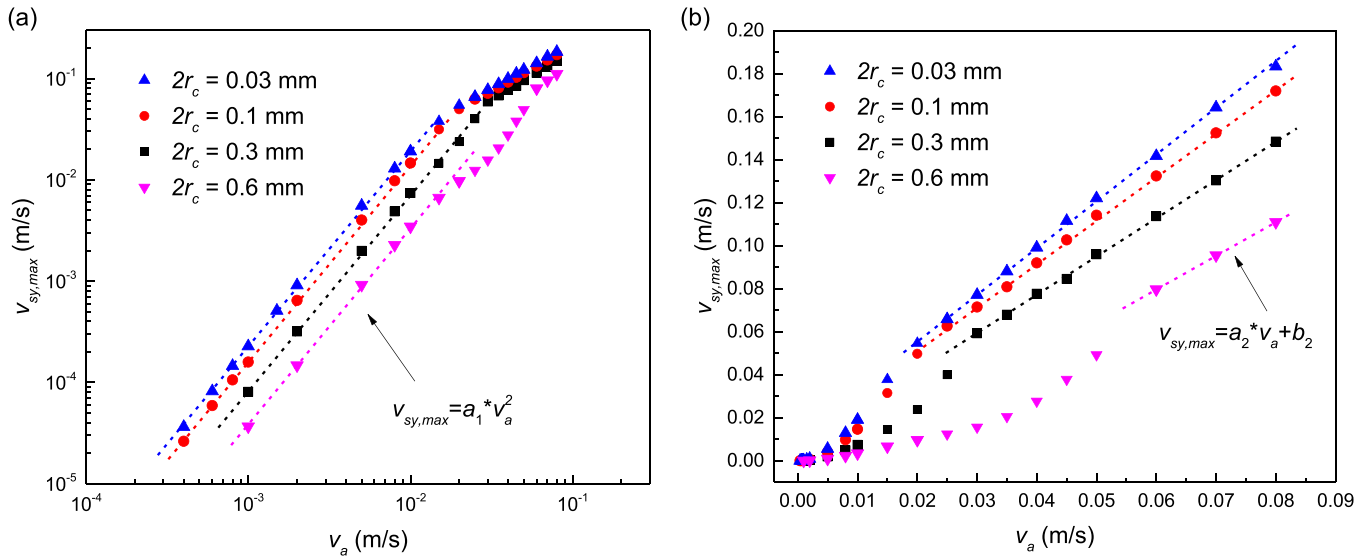

FIG. 5. Maximal streaming velocity along the y direction $v_{sy,\max}$ versus vibration velocity v_a at different tip curvature diameters $2r_c$, showing (a) quadratic dependence for low v_a, and (b) linear dependence for higher v_a, with a crossover behavior in-between. The curves show the quadratic and linear fittings. The thresholds v_{ac1} and v_{ac2} define, respectively, the upper limit of the quadratic regime and the lower limit of the linear one. The adjusted R^2 of each fitted curves are all above 0.99.

Figure 4 shows the vorticity maps of the streaming flow, corresponding to the same sets of conditions as those of Fig. 3. For relatively weak v_a or A, vorticity is mainly located in the vicinity of the sharp edge [Figs. 4(a) and 4(b)] and vanishes beyond a typical distance $\simeq\delta$ from the wall. Vorticity is evenly distributed in the two sides, and no visible sign of asymmetry appears in Figs. 4(a) and 4(b). As the vibration magnitude increases [Fig. 4(c)], the left and right symmetry of the vorticity map is broken. There appears a high intensity, small-sized vortex in one side (here in the left) and a very narrow and stretched vorticity region in the other one (here in the right) that seems advected much further from the VBL to generate a smoother, larger-sized vortex. We identify this asymmetric flow as an instability-induced regime since the vorticity is advected much further away from the tip in the right side of the sharp-edge structure than on the left side. As we shall see later, the side (right or left) of the large vortex is ruled by a complex interplay between forcing amplitude and initial conditions. Together with Fig. 3(c), this shows that the streaming flow is strongly asymmetric and strong enough to promote such a strong advection. The large-scale advection of vorticity in a streaming flow generated by large-amplitude vibrations ($A > \delta$) was already observed in a situation of an immersed vibrating cylinder [39], and predicted theoretically [40], though without such a left-right asymmetry. Therefore, this suggests there is a specific mechanism at play in the sharp-edge geometry under the above conditions. To further consolidate the validity of this flow instability, we repeated the simulations for various values of $2r_c$ (0.01 to 0.6 mm) and observed the same transition, though at different thresholds for A.

B. Maximal streaming velocity versus vibration velocity

In order to rationalize the above results, we quantitatively compare the data obtained for the different values of r_c. Therefore, we carry out extensive simulations within a large range of amplitude A (or forcing velocity v_a), from which we obtain sequences of streaming velocity and vorticity fields, like those in Figs. 3 and 4. In all simulations, the streaming flow reaches a stationary state after a transient evolution, of typical duration between 2 and 10 s (corresponding to 20 and 100 periods). Previous investigations [11,21,22] stated that a suitable quantification of SEAS flows, mainly constituted by a jet flow from the sharp tip, could be done by extracting the maximal streaming velocity along the y direction. This maximal velocity is denoted as $v_{sy,\max}$.

Figures 5(a) and 5(b) show the dependence of $v_{sy,\max}$ versus v_a in log-log scales [Fig. 5(a)] and lin-lin scales [Fig. 5(b)], for various values of r_c. Several trends can be extracted:

(i) At relatively low v_a, we notice a quadratic dependence of $v_{sy,\max}$ with v_a, $v_{sy,\max} = a_1 v_a^2$, confirming the trends observed in previous studies [11,21,22]. Thereafter, this regime is denoted as *quadratic*.

(ii) At high enough v_a, a linear dependence between $v_{sy,\max}$ and v_a is observed: $v_{sy,\max} = a_2 v_a + b_2$. The prefactor a_2 decreases with r_c, so does the offset b_2. Thereafter, this regime is denoted as *linear*.

(iii) At intermediate v_a, the dependence of $v_{sy,\max}$ on v_a shows a more complex crossover between the two aforementioned regimes.

More careful examinations of the velocity and vorticity fields show that these quantitative trends actually correspond to some extent to the transition between the flow regimes described above, in particular to the emergence of the instability with left-right symmetry breaking.

Based on the plots of Figs. 5(a) and 5(b), we extract the values of a_1, a_2, and b_2. We also extract the thresholds v_{ac1} and v_{ac2} corresponding to the limits of the quadratic and linear domains: below v_{ac1}, it is the quadratic domain and above v_{ac2}, it is the linear one. Their values are presented in Table II and Fig. 6 show the dependence of the difference of thresholds

TABLE II. The extracted threshold forcing velocity at different curvature diameters of sharp edges to identify streaming patterns. Symmetrical to asymmetrical pattern transition appears between the lower threshold v_{ac1} and upper threshold v_{ac2} (and corresponding values for γ, see definition in the Supplemental Material [38]), within which the deviations are ± 0.005 m/s. The range of forcing velocity v_a is 0–0.08 m/s.

Curvature diameter	Lower threshold		Higher threshold		Fitting coefficients		
$2r_c$ (mm)	v_{ac1} (m/s)	γ_{ac1} (–)	v_{ac2} (m/s)	γ_{ac2} (–)	a_1 (s/m)	a_2 (–)	b_2 (m/s)
0.03	0.015	1.24	0.02	1.65	196	2.15	0.013
0.1	0.015	1.05	0.025	1.75	149	2.0	0.012
0.3	0.01	0.49	0.03	1.46	75	1.78	0.007
0.6	0.015	0.50	0.06	2.00	26	1.56	0.014

$v_{ac2} - v_{ac1}$ versus $2r_c$ [Fig. 6(a)], and of fitting coefficients a_1 (in its dimensionless form $a_1 \nu/h$) and a_2 versus $2r_c/\delta$ [Fig. 6(b)].

Let us note that due to the limited amount of simulations in the crossover region, the determination v_{ac1} is subjected to some uncertainty, which we evaluated at ± 0.005 m/s. This threshold does not seem to vary much with r_c. Conversely, the values of v_{ac2} depend more significantly on r_c.

In the quadratic regime, the prefactor a_1 strongly decreases with increasing $2r_c$, and this decrease is sharper around the zone $r_c \simeq \delta$. The influence of the tip sharpness is consistent with previous studies at higher frequency [11,15,21–23]. However, contrary to previous studies, our parameter range is here extended to much larger values of relative amplitude A/δ. This enables to uncover an original left-right asymmetric flow regime shown in Figs. 3(c) and 4(c).

Therefore, let us now investigate in further details the transition to asymmetric flow. On this purpose, we quantitatively investigate the imbalance of vorticity between the left and right sides of the sharp structure. We compute the domain-averaged values of streaming vorticity, here considered as a scalar quantity through its projection Ω_z on the z axis, within a specific subdomain $\mathcal{D}$ of the computational one:

$$\Omega_{\mathcal{D}} = \langle \Omega_z \rangle_{\mathcal{D}} = \frac{1}{A_{\mathcal{D}}} \iint_{\mathcal{D}} \Omega_z(x, y)\, dx\, dy, \tag{10}$$

where $\langle \dots \rangle$ stands for the spatial averaging of the quantity between brackets and $A_{\mathcal{D}}$ the area of the considered domain. The integration domain $\mathcal{D}$ is taken as being either $\mathcal{L}$ or $\mathcal{R}$, respectively, the domains encompassing the left and right sides of the sharp edge (both domains have the same size). We define η_1 and η_2 as plausibly relevant quantities for this left-right imbalance, calculated from different expressions of the relative importance between the averaged vorticities in the right and left domains:

$$\eta_1 = \Omega_{\mathcal{R}}/(\Omega_{\mathcal{R}} + \Omega_{\mathcal{L}}), \tag{11}$$

$$\eta_2 = \Omega_{\mathcal{R}} - \Omega_{\mathcal{L}}. \tag{12}$$

Figure 7 gives these different values of $\eta_{1,2}$ versus v_a, for the case $2r_c = 0.3$ mm. The main outcome is that above a threshold (roughly equal to $v_{aT} = 0.025$ m/s for $2r_c = 0.3$ mm), the vorticity is not only advected further and diluted in the right side, but also that there is globally more vorticity

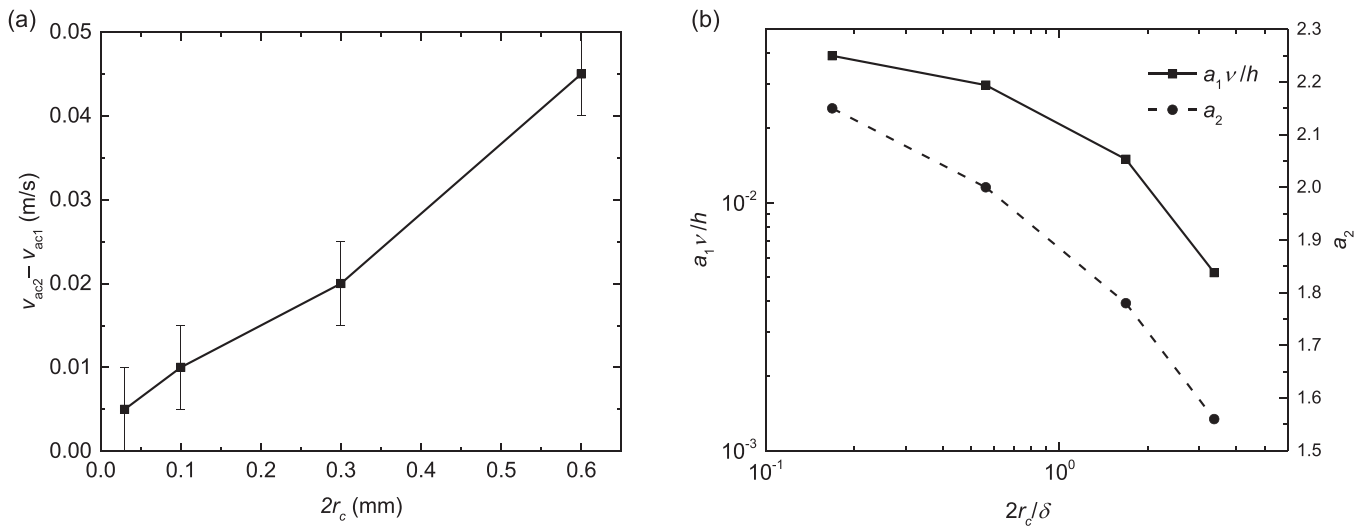

FIG. 6. (a) Difference between upper and lower thresholds (v_{ac2}-v_{ac1}) versus $2r_c$, as a measure of the crossover between quadratic and linear regimes (see text for more details). (b) Fitting coefficients a_1 (quadratic regime) plotted in its dimensionless form $a_1 \nu/h$, left axis and a_2 (linear regime), right axis, versus $2r_c/\delta$ in log-log axes.

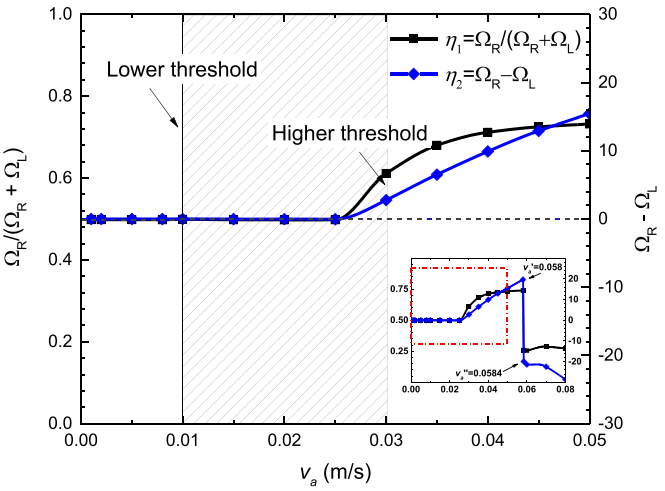

FIG. 7. Quantitative imbalance of domain-averaged vorticity between the right side ($\Omega_{\mathcal{R}}$) and the left side ($\Omega_{\mathcal{L}}$) of the sharp edge, associated to the symmetry-breaking flow instability. On the left axis, dimensionless η_1 (black squares) quantifies the relative imbalance of the streaming vorticity Ω_z between both sides ($\eta_1 = 0.5$ when symmetric). On the right axis, η_2 (blue diamonds) quantifies the absolute difference (in s^{-1}) between right and left domains ($\eta_2 = 0$ when symmetric). Black and blue lines are guide for the eye. The threshold for the appearance of the instability v_{aT} is determined at 0.026 m/s $\pm$ 0.001 m/s. The bottom right shows data in a larger range of v_a, in which the red dotted box marks the highlighted region. Beyond a value of v_a between $v_a' = 0.058$ m/s and $v_a'' = 0.0584$ m/s, a discontinuous transition to a left-side vorticity dominated flow is noticed, as η_2 jumps roughly from 20 to -20 s^{-1}. Corresponding streaming and vorticity maps are shown in Fig. 4 in the Supplemental Material [38].

in the right-side domain. The left-right imbalance increases until $v_a = 0.05$ m/s, when the averaged vorticity in the right overcomes that in the left by a factor roughly equal to 3 (as $\eta_1 \simeq 0.75$). Then, $\eta_{1,2}$ sharply decrease until $\Omega_{\mathcal{R}} < \Omega_{\mathcal{L}}$, between $v_a = 0.058$ and 0.0584 m/s (see Fig. 7 and corresponding flows in Fig. 4 in the Supplemental Material [38]). Beyond this point, the averaged vorticity remains larger in the left-side domain. It is noticeable that the flow transits from a right-side dominated vorticity to a left-side dominated one in a discontinuous manner, or in other words we could not see any symmetric flow or weakly asymmetric flow around the transitional value. Instead, the value of η_2 jumps down roughly from 20 to -20 s^{-1}.

C. Evolution of velocity field and vorticity magnitude

In order to clarify the mechanisms underlying the imbalance of streaming vorticity at relatively high forcing amplitude, we describe in more details the unsteady velocity field $\mathbf{v}_a$, especially in the vicinity of the tip where the streaming force $\mathbf{F}_s$ is supposedly strongest [7]. Figure 6 in the Supplemental Material [38] indicates the location of the points of interest, where the x and y components v_x and v_y are extracted and plotted versus time. We choose two remarkable points located at a given distance y_1 and y_2 from the tip, and at the same x coordinate (=0) at the plane of symmetry. Point 1 is taken inside the VBL ($y_1 = 0.1$ mm) while point 2 is taken outside the VBL ($y_1 = 0.5$ mm).

Figures 8 and 9 show the time evolution of v_x and v_y, respectively, for relatively weak (0.01 m/s) and strong vibration (0.05 m/s), both for $2r_c = 0.3$ mm. Let us mention that both v_x and v_y are the superimposition of the steady streaming and unsteady fields, and hence include both time-periodic and steady components. Both coordinates evolve following a transient behavior, but since the streaming flow eventually reaches a stationary state, they can be clearly identified and separated from each other once this final state is reached.

The plots cover an overall duration of 16 s, showing a time interval of 10 periods both from $t = 0$ s and from $t = 15$ s as a final state has been reached. In the final state, both the unsteady $\mathbf{v}_a$ and streaming $\mathbf{v}_s$ fields reach a stationary regime, showing a time-periodic evolution for $\mathbf{v}_a$ and a constant one for $\mathbf{v}_s$, the latter corresponding to the fully developed streaming patterns previously shown in Fig. 3.

Let us first examine the case of weak amplitude (Fig. 8). As expected, the velocity v_x exhibits a strongly dominant time-periodic and symmetric component. Let us also mention that the amplitude at the points 1 and 2, slightly larger than 0.03 m/s, is significantly stronger than the prescribed amplitude of 0.01 m/s, with comparable values in and out the VBL. This enhancement of vibration velocity near the tip, presumably a consequence of mass conservation, was already noticed in previous studies at higher frequency and smaller r_c, using a similar numerical scheme, but in the finite-element software COMSOL [21]. Let us also mention that the amplitude of v_x decreases further away from the tip (nonplotted), as it is approximately equal to 0.02 m/s at ($x = 0$ mm, $y = 1$ mm).

Regarding the y component v_y, Fig. 8(b) shows the establishment of the streaming jet from the tip, which takes roughly 10 periods (approximately 1 s), hence a time shorter than that required for the overall flow pattern to reach a steady state which is a few tens of periods (several seconds). The streaming jet finds its maximal intensity slightly outside the VBL (point 2), as it was previously noticed [22]. Furthermore, v_y has a significant oscillating component, with a phase shift of $\pi/2$ with respect to v_x, which tends to vanish outside the VBL. Interestingly, this oscillating part has a frequency equal to twice the forcing one. This is due to that the oscillating component of v_y is generated near the tip by the deflection of the v_x component, but oriented upwards whatever the direction (right or left) of v_x.

In Fig. 9, we now examine v_x and v_y under stronger forcing ($v_a = 0.05$ m/s), a situation that eventually generates to an asymmetric streaming flow [see Figs. 3(c) and 4(c)]. Within the VBL (point 1), v_x shows some departure from a purely sinusoidal function, and exhibits a second harmonic. Furthermore, the time-averaged value of v_x is nonzero, with a significant offset value, which is negative (leftward-oriented) inside and outside of the VBL, although lesser at point 2. Slightly outside the VBL, the time periodicity of v_x is rather $4\times T$. The occurrence of a second harmonic evidences what was stated before in Sec. II A, namely, that the term $(v_\omega \cdot \nabla)v_\omega$ is no longer negligible above a critical value of the forcing amplitude.

The strong asymmetry and anharmonic character is much more pronounced for v_y [see Fig. 9(b)]. While inside the VBL

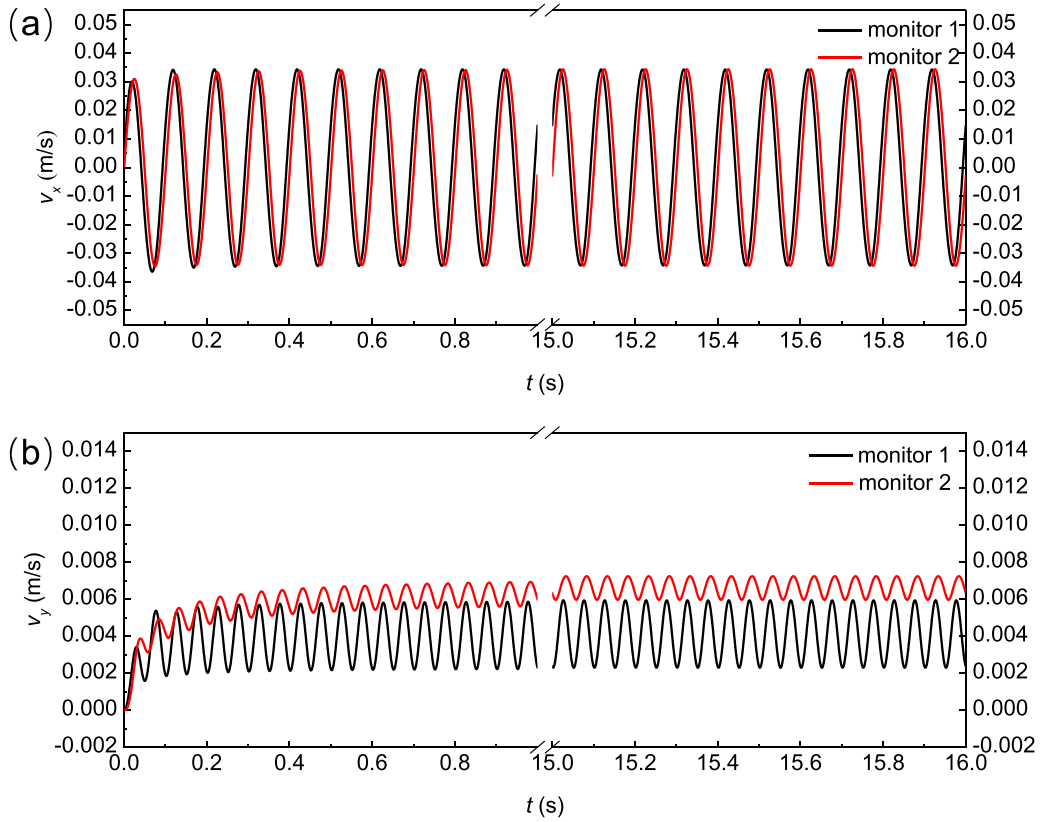

FIG. 8. Time evolution of the instantaneous velocity v with time at forcing amplitude $v_a = 0.01$ m/s, through its spatial components. (a) v_x and (b) v_y, extracted from 1–10 and 150–160 vibration periods showing, respectively, the 10 first periods and 10 later ones once a steady state is reached. The positions of monitors 1 and 2 are, respectively, 0.1 and 0.5 mm away from the tip at $x = 0$.

the behavior of v_y remains smooth with only the appearance of a higher-order harmonic, the dynamics outside the VBL shows strong fluctuations of rather high amplitude, i.e., comparable to amplitude of v_x, which was not observed at lower forcing. Although, a careful examination of the plot in the later time interval shows that these strong fluctuations have a periodic behavior, also of $4\times T$.

Let us now examine the time evolution of the imbalance of vorticity. For the quantity Ω_z, since the creation of vorticity mainly results from the powerful streaming jet shooting out from the tip, we opt to extract and plot the domain-averaged values $\Omega_{\mathcal{L}}$ and $\Omega_{\mathcal{R}}$. The cases depicted in Fig. 10 correspond to weak forcing far below the transition (a), intermediate forcing just below the transition (b), and strong forcing well above the transition (c), with forcing velocities, respectively, equal to 0.01, 0.02, and 0.05 m/s.

At weak forcing [Fig. 10(a), 0.01 m/s], the averaged vorticities $\Omega_{\mathcal{L}}$ and $\Omega_{\mathcal{R}}$ are indistinguishable from each other in both their mean value and time oscillations. Close to the onset of instability [Fig. 10(b), 0.02 m/s], one notices a slight difference in the *time-periodic* components of $\Omega_{\mathcal{L}}(t)$ and $\Omega_{\mathcal{R}}(t)$ (which both show period doubling), in the sense that $\Omega_{\mathcal{R}}(t)$ exhibits a more pronounced higher order harmonic. For $v_a = 0.05$ m/s [Fig. 10(c)], the instability is revealed by a growing imbalance between $\Omega_{\mathcal{L}}$ and $\Omega_{\mathcal{R}}$ in the first 10 periods. In the final state, the average gap between $\Omega_{\mathcal{L}}(t)$ and $\Omega_{\mathcal{R}}(t)$ is significantly larger than the mean value of $\Omega_{\mathcal{L}}(t)$ itself. Following the characteristics of the velocity components near the tip, both $\Omega_{\mathcal{L}}(t)$ and $\Omega_{\mathcal{R}}(t)$ show a more complex harmonic structure than that at moderate forcing. Also, the time oscillations of $\Omega_{\mathcal{L}}(t)$ and $\Omega_{\mathcal{R}}(t)$ exhibit a phase shift between each other.

To investigate further the mechanisms of the instability, we extracted the instationary flow field around the tip at different phases of the forcing. Figures 11–13 show these fields at successive phases, respectively, for $v_a = 0.01$, 0.02, and 0.05 m/s. In each figure, subfigures show the flow fields (a) at the beginning of the forcing ($t = 0$ s) and (b) in the final state ($t = 15$ s), and at various phases ($\pi/10$, $5\pi/10$, $9\pi/10$, $11\pi/10$, $15\pi/10$, and $19\pi/10$).

For $v_a = 0.01$ m/s (Fig. 11), the time-periodic velocity between two half-periods shows no difference between each other except during the initial period (see in particular phases $\varphi = \pi/10$ and $11\pi/10$). In the final state, the streaming flow has clearly developed which is testified by a constant component along the y direction in the tip vicinity. For $v_a = 0.02$ m/s (Fig. 12), i.e., slightly below the instability onset, the trend is roughly the same while the streaming flow is even stronger.

Above the instability threshold ($v_a = 0.05$ m/s, Fig. 13), the asymmetry clearly appears when comparing the flow fields at one phase to that half a period later. It is particularly striking that the streaming flow grows strong enough to significantly deflect the periodic forcing near the tip [see in particular the fields at $\varphi = \pi/10$ and $11\pi/10$ in Fig. 13(a)]. Consequently, the direction of the periodic forcing is strongly influenced by the streaming flow itself during the growing phase of the

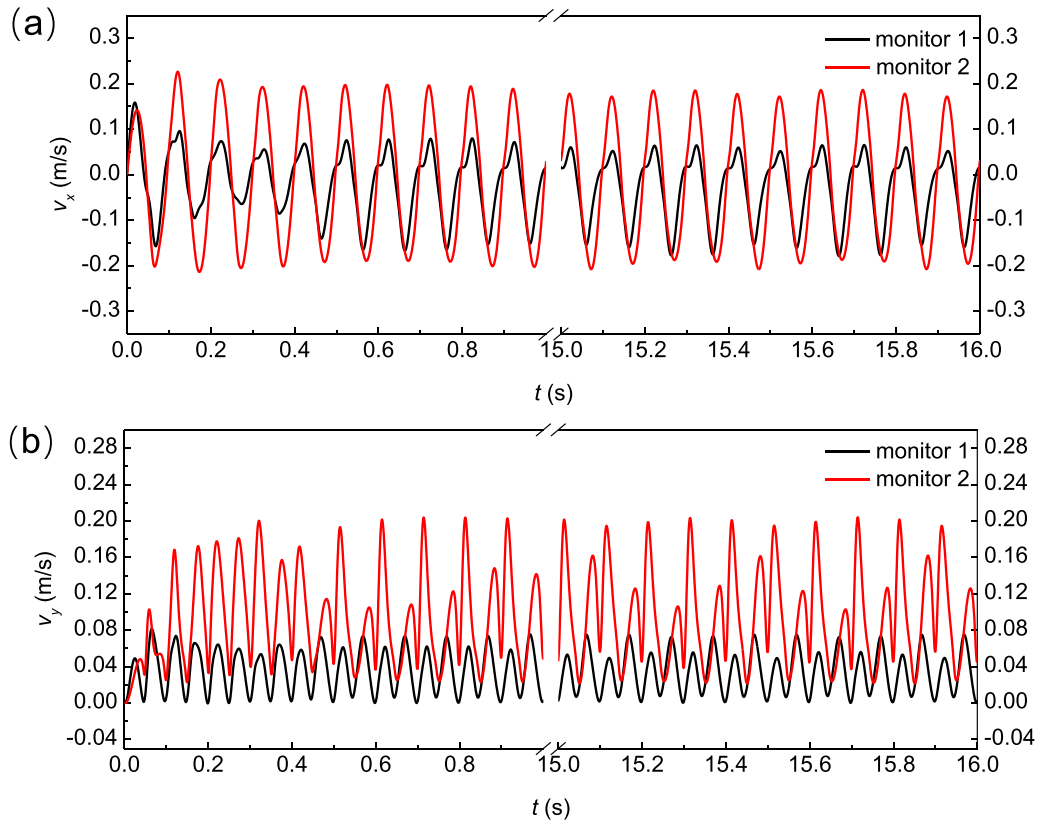

FIG. 9. Time evolution of the instantaneous velocity v with time at forcing amplitude $v_a = 0.05$ m/s, through its spatial components. (a) v_x and (b) v_y, extracted from 1–10 and 150–160 vibration periods showing, respectively, the 10 first periods and 10 later ones once a steady state is reached. The positions of monitors 1 and 2 are, respectively, 0.1 and 0.5 mm away from the tip at $x = 0$.

latter (i.e., during the very first forcing period). In other terms, during the growing phase of $\mathbf{v}_s$ (the very first periods), the temporal variations of $\mathbf{v}_s$ are strong enough to induce a significant asymmetry on $\mathbf{v}(t)$ between the half-period when the forcing is oriented right ($\varphi = 0$ to π) and the half-period when it is oriented left ($\varphi = \pi$ to 2π). In the final fields [Fig. 13(b)], a large vortex is visible at the right side of the tip. Its position slightly moves back and forth over one period, but its center remains relatively far from the tip.

These instationary flow fields are especially insightful to better understand the mechanisms of the instability. In the discussion part, we further analyze their dynamics, and provide the entire sequences as videos in the Supplemental Material [38] for four values of v_a: 0.01, 0.02, 0.05, and 0.08 m/s.

D. Energy efficiency of streaming flow

We now aim to quantify to what extent vibrations transfer their kinetic energy to the streaming flow. We define the kinetic energies associated to the whole flow and to the streaming (i.e., the time-averaged response), respectively, in Eqs. (13) and (14):

$$E_k(t) = \iint \frac{1}{2}\rho v^2(x, y, t)dx\,dy, \tag{13}$$

$$E_{k,s}(t) = \iint \frac{1}{2}\rho {v_s}^2(x, y, t)dx\,dy, \tag{14}$$

where the unit of E_k and $E_{k,s}$ is the Joule (J). In both expressions, the integration domain is the whole computational domain. The length in the z direction is taken equal to the unity, consistently with our two-dimensional model and geometry. The streaming velocity $\mathbf{v}_s$ and vorticity Ω become stationary after a duration no longer than 100 periods [see Figs. 9(b) and 10(c)]. The associated streaming kinetic energy $E_{k,s}$ is calculated for each period except for the first one.

We also determine the time-averaged kinetic energy of the overall flow, then including both time fluctuating and steady components, as

$$\langle E_k \rangle = \frac{1}{T}\int_{\tau}^{\tau+T} E_k(t)dt, \tag{15}$$

where $\langle E_k \rangle$ stands for the kinetic energy of the flow averaged over one period.

The results are shown in Figs. 14(a)–14(c), with time varying $E_k(t)$ and time averaged $\langle E_k(t) \rangle$ and $E_{k,s}(t)$. At relatively low amplitude [Fig. 14(a)], the streaming kinetic energy $E_{k,s}(t)$, shown by the red curve, converges to its final value after a duration of 10 to 20 periods. However, at higher forcing velocity, $E_{k,s}(t)$ shows a longer transient stage. Actually, what is suggested by the growth of $\langle E_k(t) \rangle$ versus time [Fig. 14(a)], is that the stationary state roughly takes 100 periods to be reached, while the examination of the velocity field near the tip (Fig. 9) rather shows a convergence after roughly 10 to 20 periods. Therefore, it is the outer part of the flow which takes a longer time to reach the steady state.

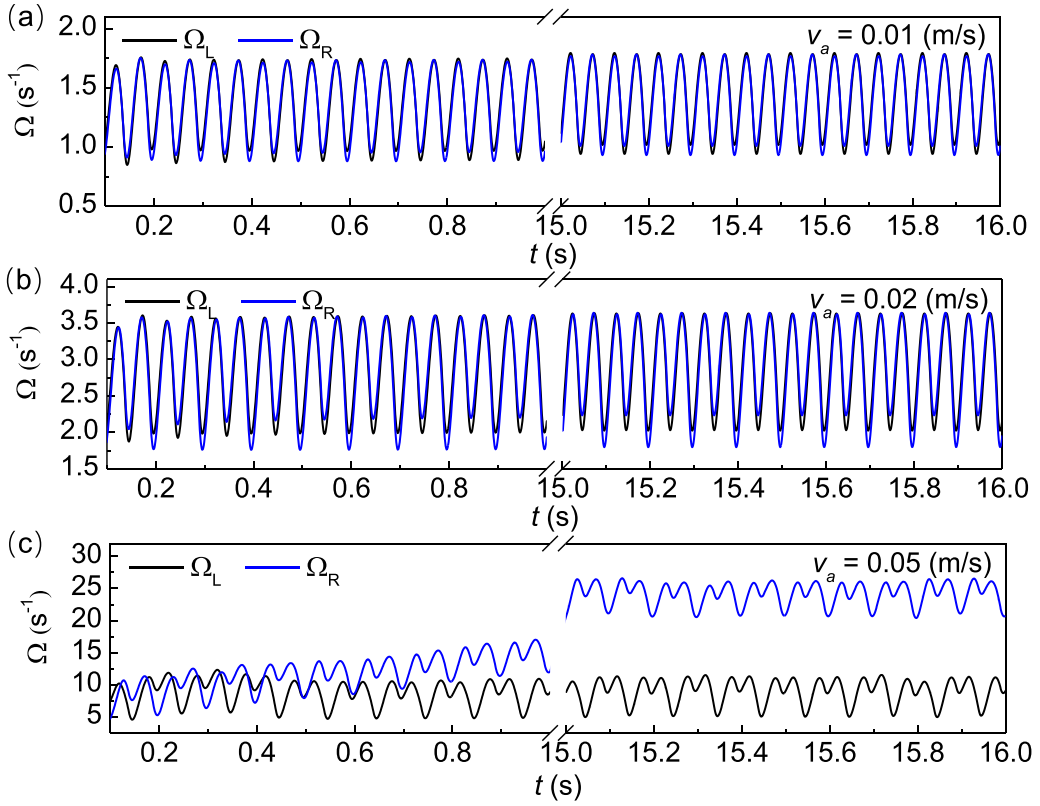

FIG. 10. Time evolution of the instantaneous vorticity, averaged within the left and right domains apart from the tip ($\Omega_{\mathcal{L}}$ and $\Omega_{\mathcal{R}}$), under various forcing velocity (a) $v_a = 0.01$ m/s, (b) $v_a = 0.02$ m/s, and (c) $v_a = 0.05$ m/s, extracted from 1–10 and 150–160 vibration periods, respectively, during the initial phase and the stationary one.

Figure 14(c) shows that the ratio of kinetic energy transfer between forcing vibrations and streaming $\langle E_k \rangle / E_{k,s}$ (plotted versus time in lin-log axes) is strongly dependent on the forcing amplitude v_a, varying by more than two orders of magnitude from $v_a = 0.01$ to 0.08 m/s (see also Table III). In terms of percentage of efficiency, at $v_a = 0.01$ m/s, the energy conversion to streaming flow represents roughly 0.37%, while at $v_a = 0.05$ m/s, it rises to 34%. This is probably the most significant result of this energy analysis, although it is unclear whether or not the instability would contribute to the increase of this ratio.

IV. DISCUSSION AND CONCLUSIONS

We here summarize the main outcomes of our study, and propose possible mechanisms to explain the unexpected appearance of an asymmetric streaming flow above a critical value of $v_a > v_{aT}$.

First, the results at relatively low forcing amplitude confirm previous ones, from both experiments and numerical simulations, obtained at higher frequency [11,21,22]. The maximal velocity in the transverse (y) direction, quantifying the streaming flow, shows a quadratic dependence with the forcing velocity ($v_{sy,\max} \sim v_a^2$) in a range of amplitudes where A remains smaller than, or of the same order as, the VBL thickness δ. Furthermore, our results confirm that a smaller value for $2r_c$ (i.e., a sharper tip) leads to a more intense streaming for the same v_a [see Fig. 6(b)]. The range of amplitude in which this quadratic dependence holds ($A < A_{c1}$) is rather independent on r_c, and lies between $A_{c1} = 0.159$ and 0.239 mm (while $\delta = 0.178$ mm for water at 10 Hz).

An original and surprising trend is noticed at higher amplitude: the streaming velocity is linearly dependent on the forcing velocity ($v_{sy,\max} \sim v_a$), which is not predicted by any previous analyses [7,21,23]. In this linear range too, the streaming flow near the tip is enhanced by the sharpness of the tip. The critical amplitude A_{c2} or velocity v_{ac2} for the appearance of the linear regime increases with r_c. While the critical amplitude A_{c2} is larger than both r_c and δ, there is no simple relationship between A_{c2} and r_c (see Table II). Our attempts to find a criterion using a dimensionless amplitude γ remains only partly conclusive too (see Supplemental Material [38]): the threshold value γ_{ac2} is between 1.46 and 1.75 for sharp edges, while it is rather close to 2 for nonsharp edge ($2r_c = 0.6$ mm). In-between quadratic and linear regimes, a crossover region is observed, which width shows a fairly linear dependence with $2r_c$ [see Fig. 6(a)].

By reconsidering Eq. (7), the quadratic regime is generally predicted by a scaling law under the assumption of $v_s \ll v_a$, then when the term $\rho(\mathbf{v}_s \cdot \nabla)\mathbf{v}_s$ is negligible. The time-averaged scaling law relating the streaming and the vibration velocity then yields

$$v_s \sim \frac{\delta^2}{\nu r_c} v_a^2$$

which is the commonly predicted relationship for classical Rayleigh streaming [6]. This is also the case for sharp-edge streaming, although this relationship was refined by

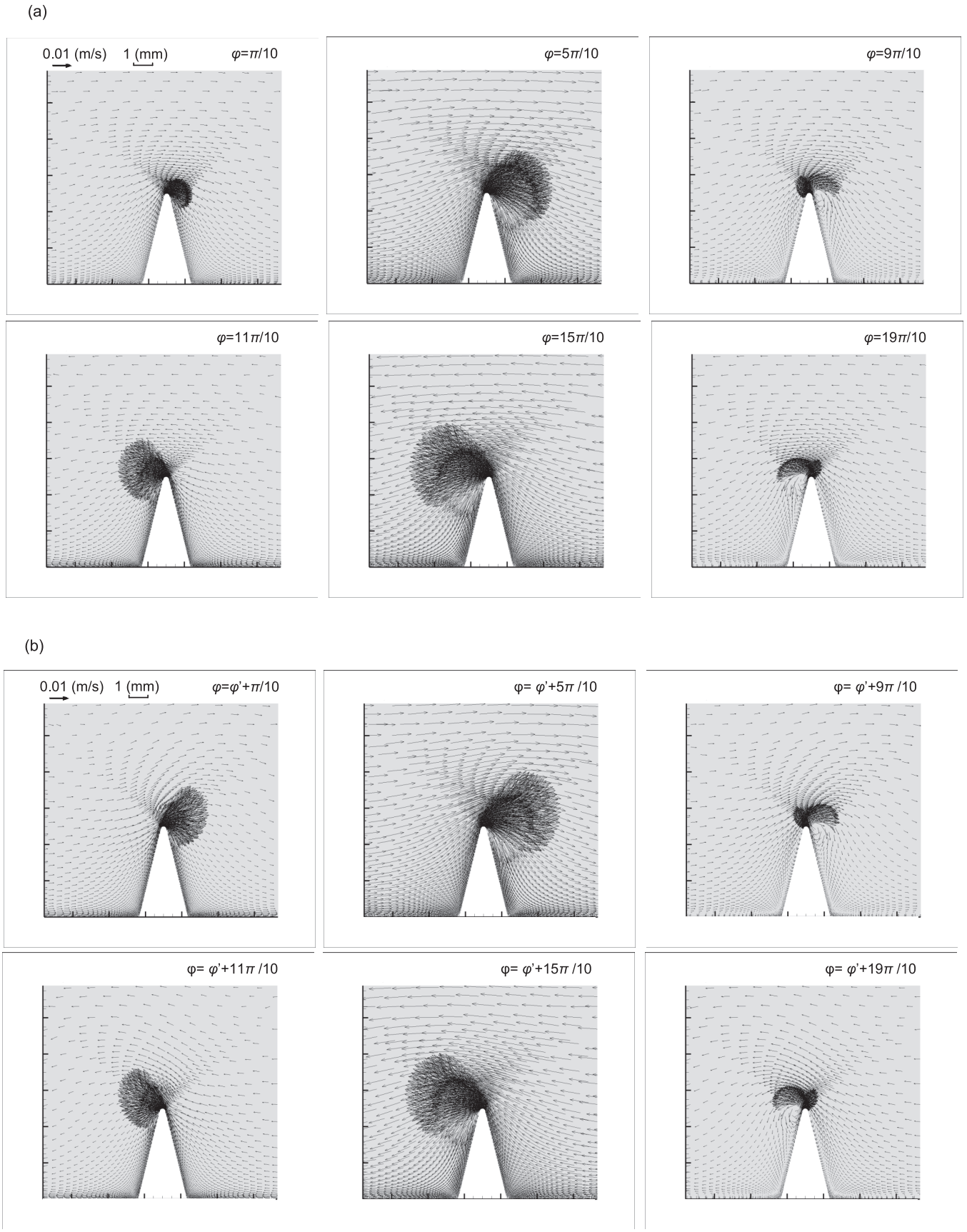

FIG. 11. Velocity fields at different phases during a forcing period. (a) Initial time $t = 0$, and (b) after fully established stationary streaming ($t = 15$ s, $\varphi' = 150\times 2\pi$). The parameters of this case are $\alpha = 30^\circ$, $2r_c = 0.3$ mm, $f = 10$ Hz, and $v_a = 0.010$ m/s.

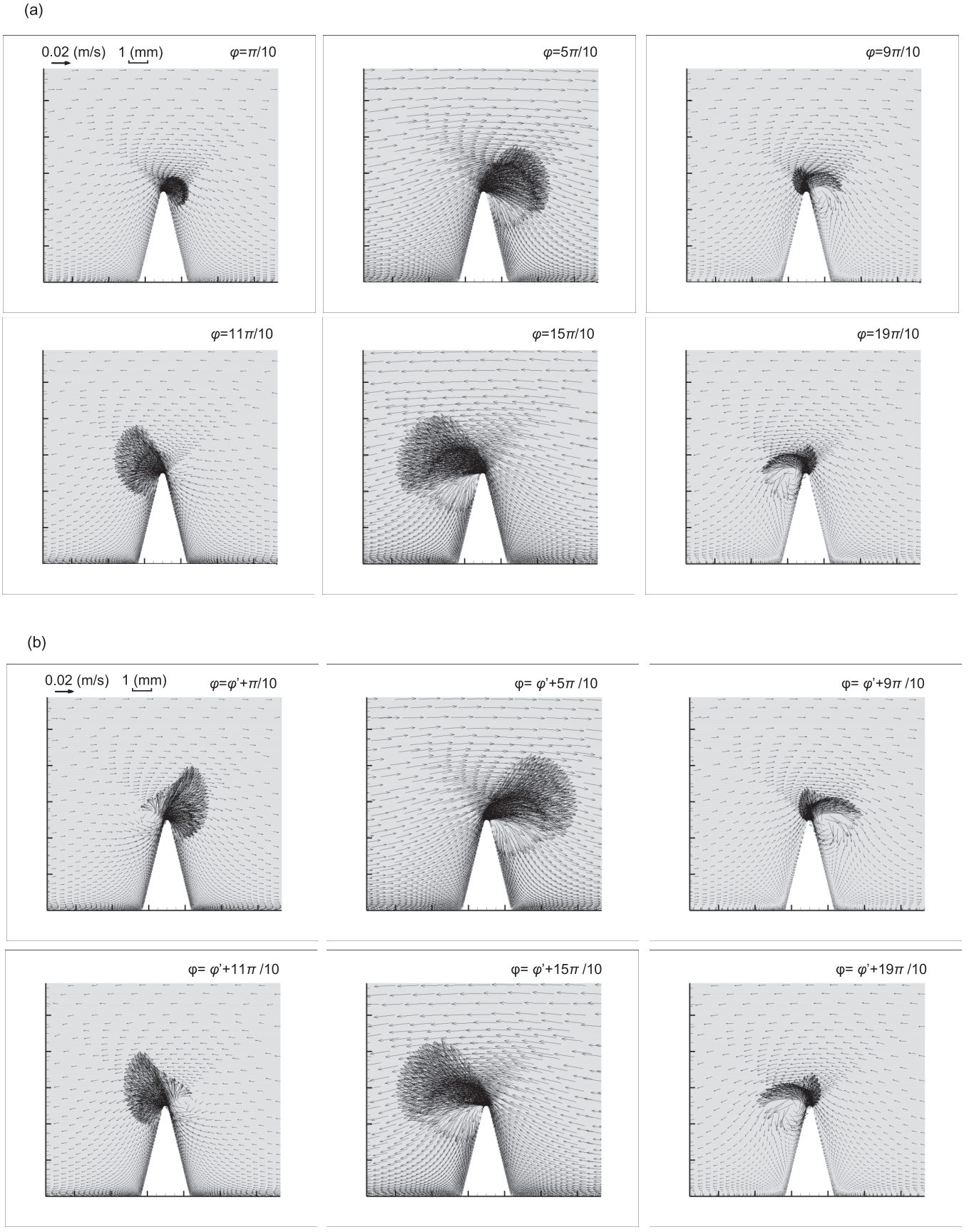

FIG. 12. Velocity field at different phases during a forcing period. (a) Initial time $t = 0$, and (b) after fully established stationary streaming ($t = 15$ s, $\varphi' = 150\times 2\pi$). The parameters of this case are $\alpha = 30^\circ$, $2r_c = 0.3$ mm, $f = 10$ Hz, and $v_a = 0.02$ m/s.

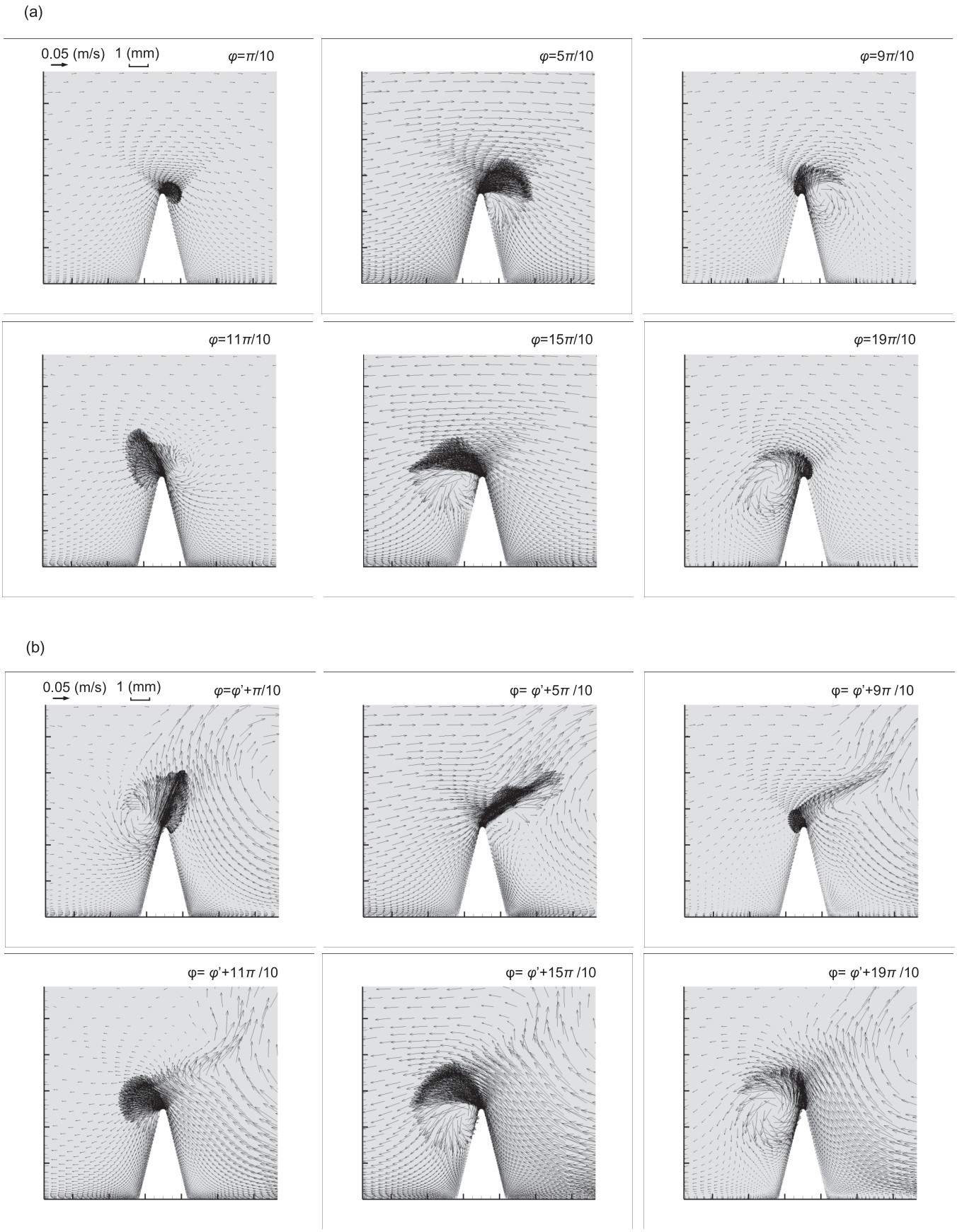

FIG. 13. Velocity field at different phases during a forcing period. (a) Initial time $t = 0$, and (b) after fully established stationary streaming ($t = 15$ s, $\varphi' = 150\times 2\pi$). The parameters of this case are $\alpha = 30^\circ$, $2r_c = 0.3$ mm, $f = 10$ Hz, and $v_a = 0.050$ m/s.

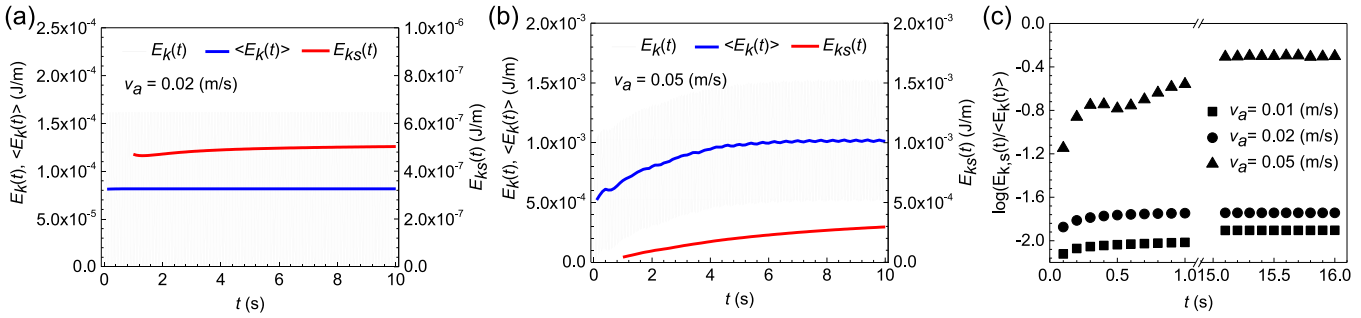

FIG. 14. (a), (b) Time evolution of kinetic energies for the whole flow (left axis, gray curve, and blue one for its time average over one period) and of the streaming flow (right axis, red curve), (a) at moderate forcing vibration ($v_a = 0.02$ m/s) and (b) relatively strong forcing vibration ($v_a = 0.05$ m/s) during the first 100 periods. The tip curvature diameter is $2r_c = 0.3$ mm. (c) Logarithm of the ratio of streaming kinetic energy over the period-averaged flow field kinetic energy, $\log \frac{E_{k,s}(t)}{\langle E_k(t)\rangle}$ versus time, under different forcing vibrations; here shown from the 1–10 and 150–160 vibration periods. Corresponding ratio at final state is also indicated in Table III.

Ovchinnikov *et al.* [7] to take into account the influence of the tip angle α and height h of the sharp structure. Hence, from Eq. (7) again, a linear relationship between v_s and v_a would suggest that the self-advective term $\rho(\mathbf{v}_s \cdot \nabla)\mathbf{v}_s$ would become dominant over the diffusive one ($\mu\nabla^2\mathbf{v}_s$). In this case, a simple scaling law between the forcing and advective streaming terms yields

$$v_s \sim \left(\frac{\delta}{r_c}\right)^{1/2} v_a$$

taking δ as the typical length scale for the variation of v_s (as it was previously shown that δ was the typical scale of decrease of v_s along the y direction) [21], while r_c is the natural length scale for the gradients of forcing velocity. Of course, this is to be taken as a coarse estimate since the velocity fields show that vorticity can be advected further away the VBL. Still below the onset of instability, the scale of variation of v_s remains indeed δ, and not h or H. Also, the typical value of v_s for the transition between quadratic and linear regimes, can be given by a comparison of the relative importance of diffusive and advective terms, which introduces the definition of a streaming Reynolds number Re_s:

$$\mathrm{Re}_s = \frac{|\mathbf{v}_s| l_s}{\nu}, \tag{16}$$

where l_s is a typical length scale taken equal to $2r_c$, while $v_{sy,\max}$ is taken as the typical value for $|\mathbf{v}_s|$. Here, r_c is taken as a natural length scale for the longitudinal variations of v_s, whereas previously the length scale δ was taken as the variations of v_s along the transverse direction. Given the values of v_{ac1} and a_1 for the different $2r_c$ (Table II), the corresponding calculated values of $v_{sy,\max}$ are 0.044, 0.033, 0.011, and 0.006 m/s, respectively, for $2r_c = 0.03$, 0.1, 0.3, and 0.6 mm. The values for Re_s are 1.3, 3.3, 3.3, and 3.6, respectively. Therefore, except for $2r_c = 0.03$ mm (for which the oscillating component is partly modified by the streaming one), the threshold where the quadratic scaling $v_{sy,\max} \sim v_a^2$ ceases to hold, seems to be ruled by a critical value of Re_s around 3. Let us note that it should also correspond to a transition from a laminar to a jetlike behavior [3].

TABLE III. Ratio of kinetic energies of the streaming over the overall flow.

Conditions	Terms	Cycle-integrated kinetic energy/J	$E_{k,s}/\langle E_k\rangle$
$v_a = 0.01$ m/s	$\langle E_k\rangle$	2.03×10^{-5}	0.0037
	$E_{k,s}$	7.49×10^{-8}	
$v_a = 0.02$ m/s	$\langle E_k\rangle$	8.16×10^{-5}	0.0063
	$E_{k,s}$	5.11×10^{-7}	
$v_a = 0.05$ m/s	$\langle E_k\rangle$	9.97×10^{-4}	0.34
	$E_{k,s}$	3.38×10^{-4}	
$v_a = 0.08$ m/s	$\langle E_k\rangle$	3.14×10^{-3}	0.43
	$E_{k,s}$	1.34×10^{-3}	

Together with the aforementioned transitions on the quantitative trends, an instability leading to left-right asymmetry in the streaming flow structure appears. Figure 7 shows the progressive occurrence of the asymmetry, with an imbalance of vorticity between the left and right sides of the tip. Although it is unclear how the departure from the aforementioned quadratic dependence would be related to the asymmetry, the latter appears close to the upper threshold $v_{aT} \simeq v_{ac2}$. In the crossover region, the flow pattern remains mostly symmetric. However, Figs. 3(a) and 3(b) illustrate the difference between two flow patterns, one being in the range of the quadratic regime [Fig. 3(a), $v_a = 0.01$ m/s] and the other one being in the one of the crossover [Fig. 3(b), $v_a = 0.02$ m/s]. At low amplitude [Fig. 3(a)], the streaming mainly consists in a strong directional jet shooting out from the tip, and creating a pair of vortices at a close distance (i.e., $< \delta$) from the tip. It is the usual flow structure for sharp-edge streaming, mostly noticed so far, and very similar to what was observed at higher frequency [7,11,15–17,21,23] [see also Fig. 2(a)]. At intermediate amplitude [Fig. 3(b)], the flow pattern is dominated by two symmetric regions of high velocity aside from the tip, while the central jet gets relatively weaker. The pair of vortices close to the tip induce large vortices of lesser intensity in an outer region further from the tip. These outer vortices are not visible in Fig. 4(b) due to the scale chosen to emphasize the intense inner vorticity, but they appear clearly as a pattern of streamlines in Fig. 3(b). Such a change in the flow pattern was previously noticed in a different situation where $r_c > \delta$ [21], with a similar departure from a quadratic relationship

between $v_{sy,\max}$ and v_a. Let us also mention the similarities with the appearance of outer streaming in the usual Rayleigh-Schlichting streaming [6], where outer vortices appear above a critical Reynolds number [39–42].

When the amplitude is increased further, the asymmetric flow pattern shows intense vorticity at a large distance ($\gg\delta$) from the tip, but on one side only. Repeating these simulations for various channel widths without any noticeable difference (see Fig. 2 in [38]) suggests that the instability is intrinsic to the flow and not induced by interactions between the flow and the opposite wall or due to other finite-size effects. Also, the preferential side for the asymmetry is ruled by initial conditions (see Fig. 1 in [38]), which suggests that the instability could be related to the interaction between the time-periodic forcing and the streaming flow, during the growing phase of the latter. This is confirmed by careful and comparative examinations of the instationary flow fields both during the first periods and during the stationary final state (see also corresponding videos in [38]). Hence, at $v_a = 0.05$ m/s, the final vorticity is more intense in the right side for $\varphi_0 = 0$ and $\pi/2$ ($\eta_1 > 0.5$) and more intense in the left side for $\varphi_0 = \pi$ and $3\pi/2$ ($\eta_1 < 0.5$) (see also Fig. 7). Conversely at $v_a = 0.08$ m/s and $\varphi_0 = 0$, the vorticity is more intense in the left side, and we also find an equivalent dependence of η_1 or η_2 on φ_0. The sequence of instationary flow fields, equivalent to Figs. 11–13, is depicted in Fig. 3 in the Supplemental Material [38].

By noticing the sensitivity to initial conditions on $\eta_{1,2}$, and that the value of v_a above v_{aT} influences the sign of $\eta_2 = \Omega_{\mathcal{R}} - \Omega_{\mathcal{L}}$, we put our focus on the growth phase of v_s during the first forcing periods. During each half-period, the forcing velocity vector $\mathbf{v}_a$ is directed alternatively toward the left and the right direction and generates both instationary vorticity past the sharp tip and steady streaming just above the tip, where the effective force F_s is supposedly the strongest [7]. At relatively weak forcing (see sequences at $v_a = 0.01$ and 0.02 m/s), the instationary vorticity remains bounded at a distance from the tip roughly equal to the VBL thickness. Furthermore, the streaming jet is not strong enough to induce a significant advection of vorticity. This is confirmed by the steady vorticity maps at low amplitude [Figs. 4(a) and 4(b)]. At higher forcing (see sequences at $v_a = 0.05$ and 0.08 m/s in Fig. 13 in the main text and in Fig. 3 and also in videos in the Supplemental Material [38]), the instationary vorticity is advected away from the tip by the strong streaming flow. We here propose that this advection could be one of the origin of the instability associated to the left-right symmetry breaking flow pattern. Indeed, during the transient phase (first forcing periods), the streaming flow increases and strengthens [see Fig. 9(b)]. Hence, during each of these first half periods of forcing, as transient vorticity is generated on each side of the tip, the growing streaming flow advects this vorticity further and further away. Therefore, the resulting time-averaged vorticity shall be asymmetric. From the sequences, one can see that this asymmetry, generated during the first periods actually influences in turn the streaming flow by deflecting it from a purely transverse jet. Hence, the sign of the vorticity imbalance seems to be determined by the phase of the forcing, then the side of the tip where instationary vorticity is generated, corresponding to the moment when v_s is growing strong enough (during the transient) for that the vortex is shed away from the VBL. This is the reason why the side of dominant vorticity is dependent on both the initial phase shift of the forcing (see Fig. 1 in [38]) but also on the value of v_a.

Let us remark that the threshold for this instability (occurring at $v_a = 0.026$ m/s for $2r_c = 0.3$ mm) corresponds to a value of the dimensionless number $\mathrm{R}_\omega = 1.38$, i.e., close to the limit where the term $(v_\omega \cdot \boldsymbol{\nabla})v_\omega$ is no longer negligible, with the emergence of nonharmonic oscillating flow especially near the tip.

A similar vortex shedding related to a synthetic jet is somewhat common in the control of boundary-layer flows, where such acoustically generated jets are rather used to prevent or delay separation and turbulence. Here, the peculiarity is that not only the boundary layer is instationary, as created by periodic forcing on a wall-bounded flow (see, e.g., Chap. 13 of [5]), but also that both instationary vorticity and directional jet come from the same origin, namely, the periodic forcing. In our study, such a coupling clearly appears considering the crossed terms $\rho(\mathbf{v}_a \cdot \boldsymbol{\nabla})\mathbf{v}_s$ and $\rho(\mathbf{v}_s \cdot \boldsymbol{\nabla})\mathbf{v}_a$ in the instationary equation of the momentum conservation (5), both terms which are generally neglected when $v_s \ll v_a$ but which here can strongly modify the spatiotemporal variations of the forcing, especially near the tip. The first term accounts for the periodic disturbances of the streaming jet, which is then deflected alternatively left and right, but also periodically pulsed up and down due to the $2f$ component of the flow response in the y direction. The second term accounts for the aforementioned advection of the instationary vorticity by the streaming flow, which is then strong enough to make this advection to dominate over the diffusive term $\mu\nabla^2\mathbf{v}_a$.

In a practical viewpoint, such unstable asymmetric flow can be sought or avoided. For instance, in the context of mixing or transfer enhancement, SEAS was shown to be an effective way to enhance mixing in microchannel flows with a periodic array of sharp structures, using the strong transverse streaming jets to perturb the mixing layer and deflect the otherwise parallel streamlines [12]. Here, not only the use of low-frequency vibrations makes our results relevant for various situations of vibration harvesting, but also the ability to exploit large enough amplitude makes it possible to generate asymmetric and initial condition-dependent streaming, for which the vorticity is advected far beyond the VBL. The potentiality to enhance transfer with such unstable asymmetric flows, when using several sharp edges or playing with a time-dependent phase shift of an anharmonic forcing, is promising.

Data may be made available upon written request to the corresponding author.

ACKNOWLEDGMENT

G. Zhong received funding from the China Scholarship Council (Grant No. 202006280281).

[1] M. Wiklund, R. Green, and M. Ohlin, Acoustofluidics 14: Applications of acoustic streaming in microfluidic devices, Lab Chip **12**, 2438 (2012).

[2] C. Eckart, Vortices and streams caused by sound waves, Phys. Rev. **73**, 68 (1948).

[3] S. J. Lighthill, Acoustic streaming, J. Sound Vib. **61**, 391 (1978).

[4] L. Rayleigh, On the circulation of air observed in kundt's tubes, and on some allied acoustical problems, Philos. Trans. R. Soc. London **175**, 1 (1884).

[5] H. Schlichting and K. Gersten, *Boundary-Layer Theory* (Springer, London, 2017).

[6] S. Boluriaan and P. Morris, Acoustic streaming: from Rayleigh to today, Int. J. Aeroacoust. **2**, 255 (2003).

[7] M. Ovchinnikov, J. Zhou, and S. Yalamanchili, Acoustic streaming of a sharp edge, J. Acoust. Soc. Am. **136**, 22 (2014).

[8] H. Liu, C. J. Tay, C. Quan, T. Kobayashi, and C. Lee, Piezoelectric mems energy harvester for low-frequency vibrations with wideband operation range and steadily increased output power, J. Microelectromech. Syst. **20**, 1131 (2011).

[9] M. A. A. Abdelkareem, L. Xu, M. K. A. Ali, A. Elagouz, J. Mi, S. Guo, Y. Liu, and L. Zuo, Vibration energy harvesting in automotive suspension system: A detailed review, Appl. Energy **229**, 672 (2018).

[10] C. Hou, T. Chen, Y. Li, M. Huang, Q. Shi, H. Liu, L. Sun, and C. Lee, A rotational pendulum based electromagnetic/triboelectric hybrid-generator for ultra-low-frequency vibrations aiming at human motion and blue energy applications, Nano Energy **63**, 103871 (2019).

[11] C. Zhang, X. Guo, P. Brunet, M. Costalonga, and L. Royon, Acoustic streaming near a sharp structure and its mixing performance characterization, Microfluid. Nanofluid. **23**, 104 (2019).

[12] C. Zhang, P. Brunet, L. Royon, and X. Guo, Mixing intensification using sound-driven micromixer with sharp edges, Chem. Eng. J. **410**, 128252 (2021).

[13] E. Izadpanah, A. Ashouri, M. Liravi, and Y. Amini, Effect of vortex-induced vibration of finned cylinders on heat transfer enhancement, Phys. Fluids **31**, 073604 (2019).

[14] J. Whitehill, A. Neild, T. W. Ng, S. Martyn, and J. Chong, Droplet spreading using low frequency vibration, Appl. Phys. Lett. **98**, 133503 (2011).

[15] P. H. Huang, Y. Xie, D. Ahmed, J. Rufo, N. Nama, Y. Chen, C. Y. Chan, and T. J. Huang, An acoustofluidic micromixer based on oscillating sidewall sharp-edges, Lab Chip **13**, 3847 (2013).

[16] N. Nama, P. H. Huang, T. J. Huang, and F. Costanzo, Investigation of acoustic streaming patterns around oscillating sharp edges, Lab Chip **14**, 2824 (2014).

[17] P. H. Huang, N. Nama, Z. Mao, P. Li, J. Rufo, Y. Chen, Y. Xie, C. H. Wei, L. Wang, and T. J. Huang, A reliable and programmable acoustofluidic pump powered by oscillating sharp-edge structures, Lab Chip **14**, 4319 (2014).

[18] A. Ozcelik, N. Nama, P.-H. Huang, M. Kaynak, M. R. McReynolds, W. Hanna-Rose, and T. J. Huang, Acoustofluidic rotational manipulation of cells and organisms using oscillating solid structures, Small **12**, 5120 (2016).

[19] N. Nama, P. H. Huang, T. J. Huang, and F. Costanzo, Investigation of micromixing by acoustically oscillated sharp-edges, Biomicrofluidics **10**, 024124 (2016).

[20] J. Lei, M. Hill, C. P. de León Albarrán, and P. Glynne-Jones, Effects of micron scale surface profiles on acoustic streaming, Microfluid. Nanofluid. **22**, 140 (2018).

[21] C. Zhang, X. Guo, L. Royon, and P. Brunet, Unveiling of the mechanisms of acoustic streaming induced by sharp edges, Phys. Rev. E **102**, 043110 (2020).

[22] C. Zhang, X. Guo, L. Royon, and P. Brunet, Acoustic streaming generated by sharp edges: experiments on the coupled influence of liquid viscosity and frequency, Micromachines **11**, 607 (2020).

[23] A. A. Doinikov, M. S. Gerlt, A. Pavlic, and J. Dual, Acoustic streaming produced by sharp-edge structures in microfluidic devices, Microfluid. Nanofluid. **24**, 32 (2020).

[24] S. Oberti, A. Neild, and T. W. Ng, Microfluidic mixing under low frequency vibration, Lab Chip **9**, 1435 (2009).

[25] J. M. R. Graham, The forces on sharp-edged cylinders in oscillatory flow at low keulegan–carpenter numbers, J. Fluid Mech. **97**, 331 (1980).

[26] L. Tao and K. Thiagarajan, Low kc flow regimes of oscillating sharp edges I. Vortex shedding observation, Appl. Ocean Res. **25**, 21 (2003).

[27] P. J. Westervelt, The theory of steady rotational flow generated by a sound field, J. Acoust. Soc. Am. **25**, 60 (1953).

[28] W. L. Nyborg, Acoustic streaming near a boundary, J. Acoust. Soc. Am. **30**, 329 (1958).

[29] N. Riley, Acoustic streaming, Theoret. Comput. Fluid Dyn. **10**, 349 (1998).

[30] J. Friend and L. Y. Yeo, Microscale acoustofluidics: Microfluidics driven via acoustics and ultrasonics, Rev. Mod. Phys. **83**, 647 (2011).

[31] H. Bruus, Acoustofluidics 2: Perturbation theory and ultrasound resonance modes, Lab Chip **12**, 20 (2012).

[32] S. S. Sadhal, Acoustofluidics 13: Analysis of acoustic streaming by perturbation methods, Lab Chip **12**, 2292 (2012).

[33] W. L. Nyborg, Acoustic streaming due to attenuated plane waves, J. Acoust. Soc. Am. **25**, 68 (1953).

[34] J. Lei, P. Glynne-Jones, and M. Hill, Comparing methods for the modelling of boundary-driven streaming in acoustofluidic devices, Microfluid. Nanofluid. **21**, 23 (2017).

[35] G. Michel and G. P. Chini, Strong wave–mean-flow coupling in baroclinic acoustic streaming, J. Fluid Mech. **858**, 536 (2019).

[36] P. K. Das, A. D. Snider, and V. R. Bhethanabotla, Acoustothermal heating in surface acoustic wave driven microchannel flow, Phys. Fluids **31**, 106106 (2019).

[37] J. T. Karlsen, P. Augustsson, and H. Bruus, Acoustic Force Density Acting on Inhomogeneous Fluids in Acoustic Fields, Phys. Rev. Lett. **117**, 114504 (2016).

[38] See Supplemental Material at http://link.aps.org/supplemental/10.1103/PhysRevE.107.025102 for additional numerical results of the asymmetric flow with different values of initial phase-shift, of channel width of tip angle, as well as details of a discontinous transition of the flow asymmetry. Also are included videos of the oscillating flow field below and above the transition to asymmetry.

[39] S. A. Bahrani, N. Perinet, M. Costalonga, L. Royon, and P. Brunet, Vortex elongation in outer streaming flows, Exp. Fluids **61**, 91 (2020).

[40] C.-Y. Wang, On high-frequency oscillatory viscous flows, J. Fluid Mech. **32**, 55 (1968).

[41] J. Holtsmark, I. Johnson, T. Sikkeland, and S. Skarlem, Boundary layer flow near a cylindrical obstacle in an oscillating incompressible fluid, J. Acoust. Soc. Am. **26**, 26 (1954).

[42] M. Tatsuno and P.-W. Bearman, A visual study of the flow around an oscillating circular cylinder at low keulegan carpenter numbers and low stokes numbers, J. Fluid Mech. **211**, 157 (1990).